

Anomalies of Cosmic Anisotropy from Holographic Universality of Great-Circle Variance

Nathaniel Selub,¹ Frederick Wehlen,¹ Craig Hogan,^{1,2} and Stephan S. Meyer¹

¹*University of Chicago, 5640 South Ellis Ave., Chicago, IL 60637*

²*Fermi National Accelerator Laboratory, Batavia, IL 60510*

We examine all-sky cosmic microwave background (CMB) temperature maps on large angular scales to test consistency with a hypothesized cosmological symmetry: a universal variance of primordial curvature perturbations on great circles. This symmetry is not a property of standard quantum inflation, but may be a natural hypothesis in a holographic model with causal quantum coherence on null surfaces. If this symmetry is assumed for primordial curvature perturbations, the amplitude and direction of the unobserved intrinsic dipole (that is, the unobserved $\ell = 1$ harmonics) can be inferred from measured $\ell = 2, 3$ harmonics by minimizing the variance of great-circle variances. It is shown that universality of great-circle variance requires unusual patterns, such as a previously noted anomalously high sectorality of the $\ell = 3$ components, and a close alignment of principal axes of $\ell = 2$ and $\ell = 3$ components. Simulations are used to show that in standard quantum inflation, only a small fraction of realizations combine dipole, quadrupole and octopole harmonics with great-circle variances as uniform as the inferred real sky. It is found that adding the intrinsic dipole leads to a nearly-null angular correlation function over the range $\Theta = [90^\circ, 135^\circ]$, in agreement with a null anti-hemispherical symmetry independently motivated by holographic causal arguments, but highly anomalous in standard cosmology. The precision of these results appears to be primarily limited by errors introduced by models of Galactic foregrounds.

I. INTRODUCTION

According to the standard cosmological model, the pattern of temperature anisotropy in the cosmic microwave background (CMB) on large angular scales approximates that of an invariant primordial scalar potential perturbation, Δ , on the surface of last scattering. Correlations of the largest angular structures provide our most direct measurement of quantum processes that lay down primordial perturbations at the earliest times.

Although the standard cosmological model agrees extraordinarily well with the angular power spectrum of the observed cosmic microwave background at scales smaller than a few degrees [1], the angular distribution on large angular scales departs considerably from expectations [2–6]. Among the well-studied “anomalies” are a remarkably small value of the two-point angular correlation function at large angles [7–9], including a near-vanishing value at $\Theta = 90^\circ$ [10]; a highly planar octopole ($\ell = 3$) component closely aligned with the quadrupole ($\ell = 2$) [11]; and a tendency for odd multipole moments to have more fluctuation power than even multipole moments [12]. In the standard model of cosmology, where the $a_{\ell m}$ components of multipole moments are predicted to be independent Gaussian random variables, the vanishing of the two-point angular correlation function near $\Theta = 90^\circ$ is anomalous at a sub-0.1% level, while the other features are each anomalous at about a one-percent level.

In the standard view, these features are all statistical flukes. However, they may be evidence of deeper underlying symmetries. In the standard model, the chance of all of these anomalies occurring simultaneously is extremely low, and there is no particular relationship between them. An alternative model of inflationary quantum states, which invokes holographic coherence on

causal inflationary horizons, creates an opportunity to connect these anomalies via new, fundamental physical symmetries [13–15]. Although standard cosmology is not significantly modified at angular scales less than a few degrees, large angles are affected by radically new correlations created by the emergence of space-time locality and causality from a quantum system. Viewed in this light, the anomalies can be seen as hints of novel correlations from quantum gravity that have not been included in the standard scenario.

Predicted correlations of primordial perturbations depend on untested assumptions about the quantum coherence of geometrical states. In the standard quantum inflation model, zero-point fluctuations of coherently quantized scalar field modes produce a universal 3D power spectrum of primordial scalar curvature perturbations on surfaces of constant time. By contrast, if quantum space-time is holographic in the sense suggested by some formal studies [16–18], non-localized quantum states of geometry may be coherent on spherical bounding surfaces of causal diamonds defined by world lines of measurements. In holographic inflation, these spherical surfaces are defined by causally coherent inflationary horizons around every observer, which can lead to a 2D power spectrum of relic perturbations on comoving spheres that obeys constraints in the angular domain with no cosmic variance. A model of this kind creates nonlocal (but still causal) correlations on large angular scales that seem conspiratorial in the standard picture. They arise from quantum non-locality on causal horizon surfaces, an effect not included in a standard scenario based on coherent quantum field states.

The holographic scenario naturally leads to the conjecture that the two-point angular correlation function of Δ on 2-spheres approximates a function constrained

by causal entanglements of horizons. This hypothesis appears to agree with symmetries of the observed angular correlation on large angular scales, in particular, the near-vanishing of angular correlation at angular separation $\Theta \geq 90^\circ$ [15].

However, symmetries of the two-point angular correlation function do not directly address anomalies of shape and orientation determined by the phases of spherical harmonic components, which do not affect the two-point angular correlation function. In principle, holographic quantum gravity can create surprising symmetries that constrain relationships between these components, again from causal coherence of quantum-gravitational states on null surfaces. For example, according to one form of the holographic scenario [15], local invariant scalar curvature at a point is determined by a coherent quantum state of its past light cone, while relationships with a definite spatial direction are governed by the state of a normal null plane. In this scenario, great circles have a special causal significance, since they delineate boundaries of coherent causal entanglement. A great circle on a sphere is the intersection of two null surfaces that carry relational information, a null plane (or infinitely large null sphere), and a light cone with an apex at the center of the sphere. These simple geometrical relationships suggest that the emergence of space-time locality may lead to universal properties of relic curvature variance on great circles. Here, we investigate the hypothesis that *any great circle has the same one-point correlation function as any sphere*, or equivalently, *the one-point variance $\langle \Delta^2 \rangle$ has a universal value for any great circle*.

Great-circle variances depend on aspects of the cosmic pattern that do not affect the two-point angular correlation function, such as the shapes and orientations of the spherical harmonic components. In general, the total variance increases with resolution or harmonic cutoff scale ℓ , so it is dominated by the smallest angular scales. Its variation is fractionally largest in skies filtered at low ℓ , where the number of components is relatively small, so the effect of any new symmetry should manifest most conspicuously at low ℓ .

Holographic symmetries of CMB temperature must be tested indirectly, because exact angular symmetries of Δ are contaminated by measurement limitations. An important limitation at large angles is Galactic foreground emission, which is imperfectly subtracted and leaves large-scale, non-primordial patterns in the maps. This aspect of the measurement can be improved with better data and models of all sky anisotropy over a wide range of frequencies.

Another limitation arises because one of the universal components is the intrinsic cosmic dipole anisotropy, which is not measurable, even in principle, from CMB data alone. Since the measured cosmic dipole is dominated by a kinetic dipole from our peculiar velocity that is several orders of magnitude larger than the predicted intrinsic dipole, it is not possible to directly measure the orientation and amplitude of the true intrinsic dipole.

Yet, the intrinsic dipole affects all-sky primordial symmetries: for example, it changes the two-point angular correlation function [15] by adding a term proportional to $\cos(\Theta)$, with a positive coefficient, and also contributes to variances on great circles.

In the standard picture, there is no correlation among different spherical harmonics; the amplitudes of individual harmonic components are independent random variables. By contrast, holographic causal entanglement among spherical horizons requires causal correlations among low order spherical harmonic components. A causal constraint on the distribution of great circle variances implies a relationship between the intrinsic (unmeasured) $\ell = 1$ dipole component and the measured $\ell = 2$ and $\ell = 3$ components. Since the dipole is characterized by just three numbers, an amplitude and a direction, it is possible to infer them from the measured components.

Thus, a universal great-circle symmetry can be tested with measurements on a single sphere, such as the large-scale surface mapped by the CMB. In this paper, we use simulated skies to explore whether there is evidence for the posited symmetry in the real sky. We study its consistency with the data, with predicted realizations of the standard model, with causal symmetries of the two-point angular correlation function, and with measured anomalies of multipole shape and orientation.

A. Overview of results

According to our holographic hypothesis, higher harmonics ought to smooth out variations of great-circle variance from lower harmonics. This behavior is manifest in the lowest harmonics of the real sky. Figs. (1) and (2) show measured $\ell = 2$ and $\ell = 3$ distributions, along with an added “inferred” intrinsic dipole that comes closest to constant variance on great circles. The Mollweide projections (Fig. 1) use standard Galactic coordinates, while the axis adopted for the equirectangular (Cartesian) projections (Fig. 2) is that defined by the inferred dipole. These projections show the high sectorality (see Eq. (8)) and alignment of the $\ell = 2$ and $\ell = 3$ distributions, and help visualize how these properties reduce variations of great-circle variance.

Thus, imposing a small variance of great-circle variances on the $\ell \leq 3$ sky, for the fixed angular power spectrum as measured, tends to require previously noted anomalies of multipole shape. In particular, the principal axis of the intrinsic dipole tends to be closely aligned with those of the quadrupole and octupole components, and the octupole pattern tends to be highly sectoral.

Simulations show that the measured distribution of great circle variances, as well as the inferred dipole amplitude and total large-angle correlation, are atypical compared with random realizations predicted by the standard quantum model of inflation (Figs. 3, 4).

Remarkably, we find that the amplitude of the intrinsic

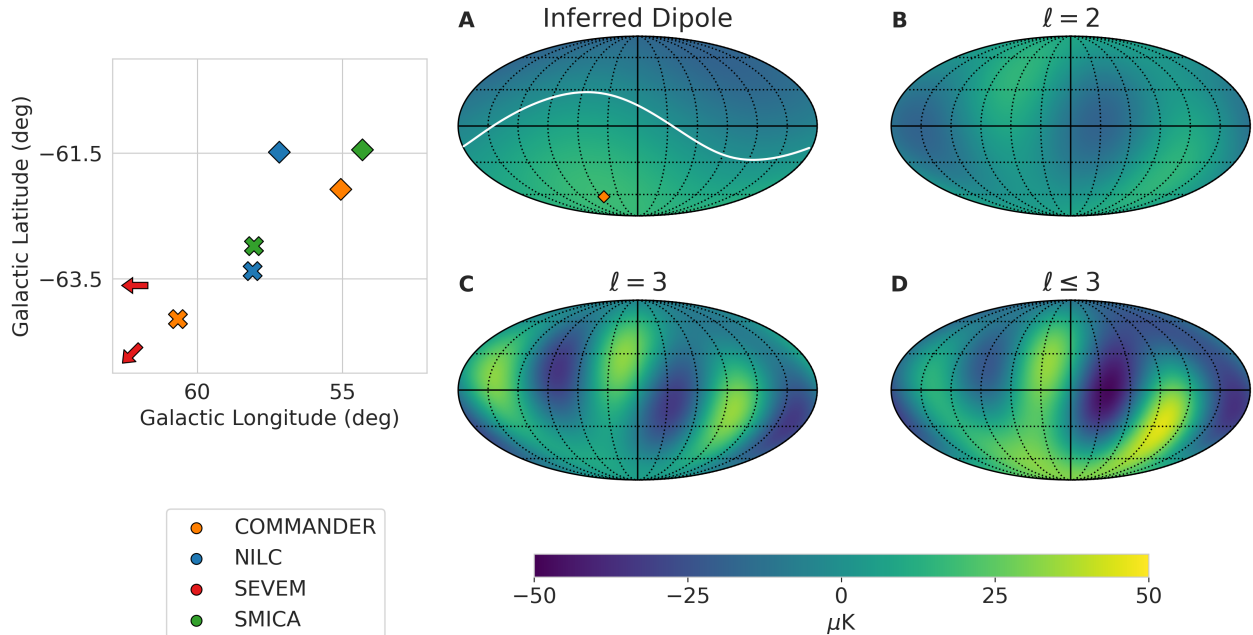


FIG. 1. On the left, an equirectangular (Cartesian) projection of a region of the sky showing the inferred dipole axis $\hat{\Omega}_I$ (diamonds) and octupole axis of maximum sectorality \hat{N}_3 (crosses) in Galactic coordinates for the *Planck* pipelines Commander, NILC, and SMICA. The axes for SEVEM lie outside the region and are instead pointed to with arrows; its $\hat{\Omega}_I$ is located at $(l, b) \approx (83.1^\circ, -63.6^\circ)$, and its \hat{N}_3 is located at $(l, b) \approx (67.1^\circ, -66.4^\circ)$, where l and b denote Galactic longitude and latitude, respectively. On the right (labeled A to D), four Mollweide projections of the low ℓ harmonic components of the inferred version of Commander are shown in Galactic coordinates. [Panel A]: The inferred dipole ($\ell = 1$) for Commander, annotated with the inferred dipole axis $\hat{\Omega}_I$ (orange diamond) and inferred dipole equator (white line), which are used to define the natural coordinate system of Commander. [Panel B]: The quadrupole ($\ell = 2$) of Commander. [Panel C]: The octupole ($\ell = 3$) of Commander. [Panel D]: The inferred version of $\ell \leq 3$ Commander, obtained by summing its octupole, quadrupole, and inferred dipole.

dipole that optimizes constant variance on great circles for measured sky maps agrees with the value [15] that approximately cancels the measured two-point angular correlation function over a wide angular interval. With this dipole, the “true” angular correlation in the range $\Theta = [\gtrsim 90^\circ, \lesssim 135^\circ]$ appears to be consistent with zero up to foreground subtraction errors, as expected from antihemispherical causal relationships in a holographic model. We show with simulations that this result is highly anomalous in standard cosmology (Figs. 5, 6), where it requires a fine-tuning of spectral amplitudes over a wide range of ℓ in the harmonic domain.

II. FRAMEWORK AND DEFINITIONS

A. Variances of great circles

The standard cosmological model predicts that on large angular scales, in the Sachs-Wolfe approximation, the $a_{\ell m}$ coefficients of the spherical-harmonic decomposition of the CMB sky are Gaussian distributed random variables with fixed variances. In this view, the observed

power spectrum is one of many realizations of the model, which is statistical in nature.

A holographic model of inflation may produce an angular power spectrum that is universal, i.e., the total variance of fluctuation power, proportional to the summed variances of $a_{\ell m}$ ’s at each ℓ in our sky, is the only one that could result from any physical realization. In this case, the phases of the $a_{\ell m}$ coefficients carry all the variation between different realizations, and contain additional information that encode higher-order correlations.

Since we have only one realization of the sky, we seek evidence for particular higher-order symmetries by comparing anomalies of our sky to those of simulated realizations that have the same angular power spectrum. We posit and test a simple symmetry, that *the variance of Δ on great circles is a constant*, or equivalently, that *the variance of great-circle variances σ_V^2 vanishes*, i.e.,

$$\sigma_V^2 = 0. \quad (1)$$

Total variance is dominated by the smallest angular scale structure, so there is relatively little difference between holographic and standard pictures at high angular resolution. The clearest signature of a new symmetry in

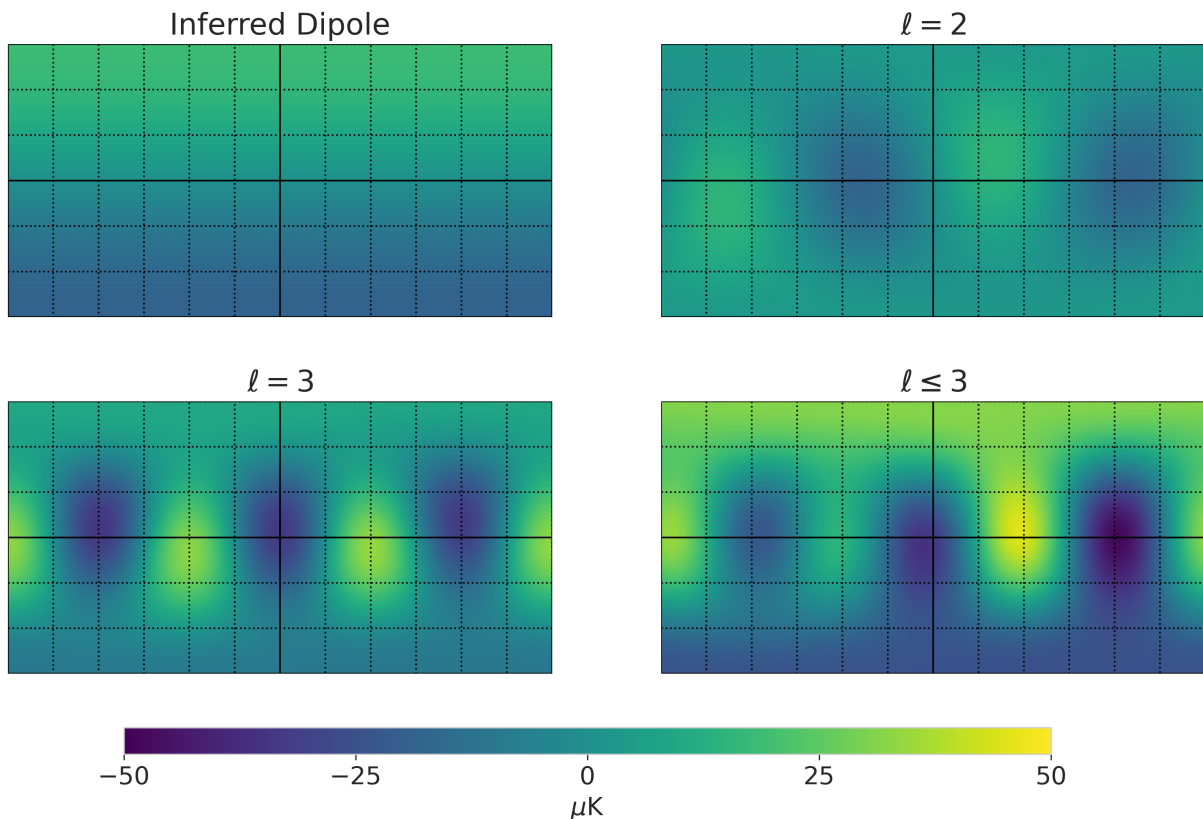


FIG. 2. Equirectangular (Cartesian) projections of the low ℓ harmonic components of the inferred version of Commander, shown in its natural coordinate system. In the natural coordinate system, the positive pole of $\mathcal{D}_{\mathcal{T}}$ coincides with \hat{z} and the $m = \ell$ harmonic coefficient $a_{3,3}$ of the octupole moment is real and positive. [Top Left]: The inferred dipole for Commander. [Top Right]: The quadrupole ($\ell = 2$) of Commander. [Bottom Left]: The octupole ($\ell = 3$) of Commander. [Bottom Right]: The inferred version of $\ell \leq 3$ Commander, obtained by summing its octupole, quadrupole, and inferred dipole. These maps show how the alignment and sectorality of the ($\ell = 2$) and ($\ell = 3$) components are related to the inferred intrinsic dipole. On the inferred dipole, the great circles that intersect the dipole's poles all have the same, maximal V_i , while the equatorial and near-equatorial great circles have null V_i and very small V_i , respectively. The highly sectoral ($\ell = 2$) and ($\ell = 3$) components aligned with the inferred dipole create variance along the equatorial and near-equatorial great circles, reducing variations of great-circle variance.

σ_V^2 is that the sky should have anomalously low σ_V^2 at low resolution, that is, including multipole moments of the spherical-harmonic decomposition of δT only up to some small ℓ cutoff. Here, we study the great-circle variances from only the lowest multipole components, $\ell = 1, 2, 3$.

On angular scales larger than a few degrees $\ell \lesssim 30$, the cosmological part of the anisotropy is dominated by the Sachs-Wolfe effect. Its structure approximates a direct map of the primordial scalar curvature Δ on the surface of last scattering, so it preserves the original pattern created by quantum inflation. We include higher resolution structure up to $\ell = 30$ when evaluating the effect of the $\ell = 1, 2, 3$ components on the overall correlation function.

B. Harmonic analysis

Given a CMB temperature map \mathcal{M} , let $\delta T(\hat{\Omega})$ denote the CMB temperature deviation from the overall mean as

a function of position on the sky, where $\hat{\Omega}$ is determined by the polar angle θ and azimuthal angle φ ,

$$\hat{\Omega} = (\theta, \varphi). \quad (2)$$

δT can be expanded as a linear combination of spherical harmonics $Y_{\ell m}$,

$$\delta T(\theta, \varphi) = \sum_{\ell=0}^{\infty} \sum_{m=-\ell}^{m=+\ell} a_{\ell m} Y_{\ell m}(\theta, \varphi), \quad (3)$$

where the $a_{\ell m}$ are harmonic coefficients constrained by the relationship

$$a_{\ell, -m} = (-1)^m (a_{\ell, m})^* \quad (4)$$

since δT is real. The angular power spectrum C_ℓ of δT is given by

$$C_\ell = \frac{1}{2\ell + 1} \sum_{m=-\ell}^{m=+\ell} |a_{\ell m}|^2, \quad (5)$$

which we can use to analytically compute the two-point angular correlation function $C(\Theta)$ of δT as

$$C(\Theta) = \frac{1}{4\pi} \sum_{\ell=0}^{\infty} (2\ell+1) C_{\ell} P_{\ell}(\cos \Theta), \quad (6)$$

where the P_{ℓ} are the Legendre polynomials.

We define the dipole component $\mathcal{D}(\theta, \varphi)$ of δT as

$$\mathcal{D}(\theta, \varphi) = \sum_{m=-1}^{m=+1} a_{1,m} Y_{1,m}(\theta, \varphi). \quad (7)$$

\mathcal{D} is uniquely determined by the location $\hat{\Omega}$ of its positive pole and the amplitude C_1 of its angular power spectrum term. Additionally, given the map \mathcal{M} , we define the map \mathcal{M}' as a version of \mathcal{M} with its dipole set to zero, and we define the $\ell \leq n$ version \mathcal{M}_n of \mathcal{M} as a version of \mathcal{M} whose δT has $C_{\ell} = 0$ for $\ell > n$.

Let \hat{n} denote the direction of the z -axis of the coordinate system in which the spherical-harmonic decomposition of δT was performed. Then, we define the *sectorality* $\mathcal{S}_{\ell}(\hat{n})$ of each multipole in this coordinate system as

$$\mathcal{S}_{\ell}(\hat{n}) = \sum_{m=-\ell, \ell} m^2 |a_{\ell m}|^2. \quad (8)$$

For each multipole, except $\ell = 0$, we define the *axis of maximum sectorality* \hat{N}_{ℓ} as the direction of the z -axis in the coordinate system in which \mathcal{S}_{ℓ} is maximized for that particular multipole. Sectorality is similar to another coordinate system dependent statistic, planarity, which is defined as

$$\sum_{m=-\ell}^{m=+\ell} m^2 |a_{\ell m}|^2. \quad (9)$$

For highly sectoral multipoles, the axis that maximizes planarity is very close to the axis of maximum sectorality, since the maximization of planarity is dominated by the $m = \pm\ell$ terms of the sum in the statistic's definition.

C. Variance of great-circle variances

For each great circle c_i , let δT_i denote the distribution of $\delta T(\hat{\Omega})$ on c_i . We define the *great-circle variance* V_i for each c_i as

$$V_i \equiv \sigma^2(\delta T_i) = \frac{1}{2\pi} \oint_{c_i} \left[\delta T(\hat{\Omega}) - \mu(\delta T_i) \right]^2 d\hat{\Omega}, \quad (10)$$

where

$$\mu(\delta T_i) = \frac{1}{2\pi} \oint_{c_i} \delta T(\hat{\Omega}') d\hat{\Omega}'. \quad (11)$$

There exists a distribution V of all such V_i calculated for each c_i , and we define the *variance of great-circle variances* σ_V^2 as

$$\sigma_V^2 \equiv \sigma^2(V). \quad (12)$$

D. Inferred dipole

We define the *inferred dipole* of \mathcal{M} as the dipole $\mathcal{D}_{\mathcal{I}}(\mathcal{M})$ that minimizes $\sigma_V^2(\mathcal{M}'_3 + \mathcal{D})$, i.e., $\mathcal{D}_{\mathcal{I}}(\mathcal{M})$ satisfies

$$\sigma_V^2(\mathcal{M}'_3 + \mathcal{D}_{\mathcal{I}}(\mathcal{M})) \leq \sigma_V^2(\mathcal{M}'_3 + \mathcal{D}) \quad (13)$$

for all possible \mathcal{D} . The location of the positive pole and the amplitude of the angular power spectrum term of $\mathcal{D}_{\mathcal{I}}(\mathcal{M})$ are denoted as $\hat{\Omega}_{\mathcal{I}}(\mathcal{M})$ and $C_{\mathcal{I}}(\mathcal{M})$, respectively. Next, we define the *inferred version* of \mathcal{M} (inferred \mathcal{M}) as the map

$$\mathcal{I}(\mathcal{M}) \equiv \mathcal{M}' + \mathcal{D}_{\mathcal{I}}(\mathcal{M}). \quad (14)$$

Finally, we define the *natural coordinate system* of \mathcal{M} as the coordinate system in which the positive pole of $\mathcal{D}_{\mathcal{I}}$ coincides with \hat{z} and the $m = \ell$ harmonic coefficient $a_{3,3}$ of its octupole moment is real and positive.

E. Standard Model realizations

Let C_{ℓ}^{SM} denote the theoretical power spectrum predicted by the standard model. We define a *standard model realization* as a CMB temperature map whose harmonic coefficients $\tilde{a}_{\ell m}$ are generated in the following manner. For each ℓ , $2\ell + 1$ numbers are chosen from a normal distribution with zero mean and variance C_{ℓ}^{SM} . Then, these numbers are used to create one real coefficient $\tilde{a}_{\ell,0}$ and ℓ complex coefficients $\tilde{a}_{\ell m}$ for $m = 1, 2, \dots, \ell$, composed of ℓ real and ℓ imaginary components. By Eq. (4), the coefficients $\tilde{a}_{\ell m}$ for $m = -1, -2, \dots, -\ell$ are also determined.

F. Standard Model dipole

A standard model intrinsic cosmic dipole $\mathcal{D}_{\mathcal{S}}$ is generated by choosing three numbers from a normal distribution with zero mean and variance C_1^{SM} . These numbers are respectively assigned to the real coefficient $\beta_{1,0}$ and the real and imaginary components of the complex coefficient $\beta_{1,1}$. By Eq. (4), the coefficient $\beta_{1,-1}$ is also determined.

G. Same-spectrum realizations

Let \mathcal{M} be a CMB temperature map with angular power spectrum α_{ℓ} . We define a *same-spectrum realization* of \mathcal{M} as a CMB temperature map with angular power spectrum $\tilde{\alpha}_{\ell}$ identical to the spectrum α_{ℓ} , and harmonic coefficients $\tilde{\mathcal{A}}_{\ell m}$ generated in the following manner. For each ℓ , $2\ell + 1$ numbers are chosen from a normal distribution with zero mean and variance α_{ℓ} . Then, these numbers are used to create one real coefficient $\mathcal{A}_{\ell,0}$ and ℓ

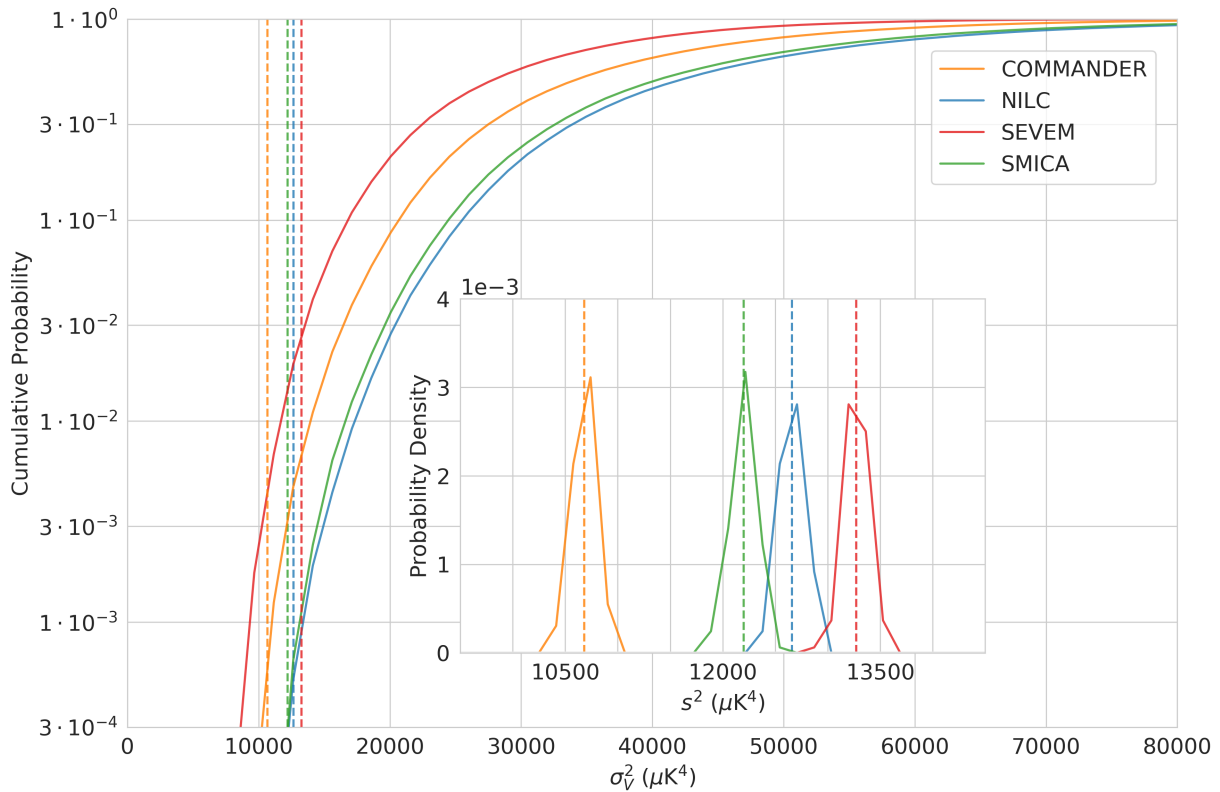


FIG. 3. The variance of great-circle variances σ_V^2 for each $\ell \leq 3$ *Planck* map with its inferred dipole added is compared against σ_V^2 for 100,000 same-spectrum realizations of that particular map. Each inferred $\ell \leq 3$ *Planck* map's set of realizations is used to create a cumulative distribution function, and at each point on this function, the cumulative probability density is the proportion of same-spectrum realizations of each inferred $\ell \leq 3$ *Planck* map with values of σ_V^2 less than the value of σ_V^2 at that point. The inset shows the spread in sample variance s^2 for each inferred $\ell \leq 3$ *Planck* map, calculated from 100 different sets of 20,000 uniformly distributed random great circles. In both plots, the vertical lines indicate the value of σ_V^2 for each inferred $\ell \leq 3$ *Planck* map, calculated as the mean value of s^2 from each map's spread of sample variances. Thus, even among realizations constrained to have the measured inferred angular power spectrum spectrum, only a small fraction of standard model realizations have great-circle variances as uniform as those of the real sky with its inferred dipole added.

complex coefficients $\mathcal{A}_{\ell m}$ for $m = 1, 2, \dots, \ell$, composed of ℓ real and ℓ imaginary components. By Eq. (4), the coefficients $\mathcal{A}_{\ell m}$ for $m = -1, -2, \dots, -\ell$ are also determined. Finally, we define the $\tilde{\mathcal{A}}_{\ell m}$ as

$$\tilde{\mathcal{A}}_{\ell m} \equiv \mathcal{A}_{\ell m} \sqrt{\frac{\alpha_\ell(2\ell+1)}{\sum_{m'=-\ell}^{m'+\ell} |\mathcal{A}_{\ell m'}|^2}}, \quad (15)$$

and these satisfy Eq. (4) by construction. Therefore, we have

$$\tilde{\alpha}_\ell = \frac{1}{2\ell+1} \sum_{m=-\ell}^{m=+\ell} |\tilde{\mathcal{A}}_{\ell m}|^2 \quad (16)$$

$$= \frac{1}{2\ell+1} \cdot \frac{\alpha_\ell(2\ell+1)}{\sum_{m'=-\ell}^{m'+\ell} |\mathcal{A}_{\ell m'}|^2} \cdot \sum_{m=-\ell}^{m=+\ell} |\mathcal{A}_{\ell m}|^2 \quad (17)$$

$$= \alpha_\ell, \quad (18)$$

so both \mathcal{M} and its same-spectrum realization have the same angular power spectrum (equivalently, two-point

angular correlation function), while, in general, looking very different in temperature space.

III. METHOD

A. Data

Our analysis is based on foreground-corrected maps of the CMB temperature from the the third public release database of the *Planck* satellite. For this paper, we used the python wrapper for the Hierarchical Equal Area iso-Latitude Pixelization (*HEALPix*) scheme [19] on maps at a resolution defined by $N_{\text{side}} = 256$. We preprocessed the *Planck* maps by downgrading them to this resolution and removing their respective monopole and dipole spherical harmonic moments. Furthermore, we consider all *Planck* maps in parallel by conducting all measurements and operations on each *Planck* map independently. In each figure, we adopt the spread of all curves as an estimate of

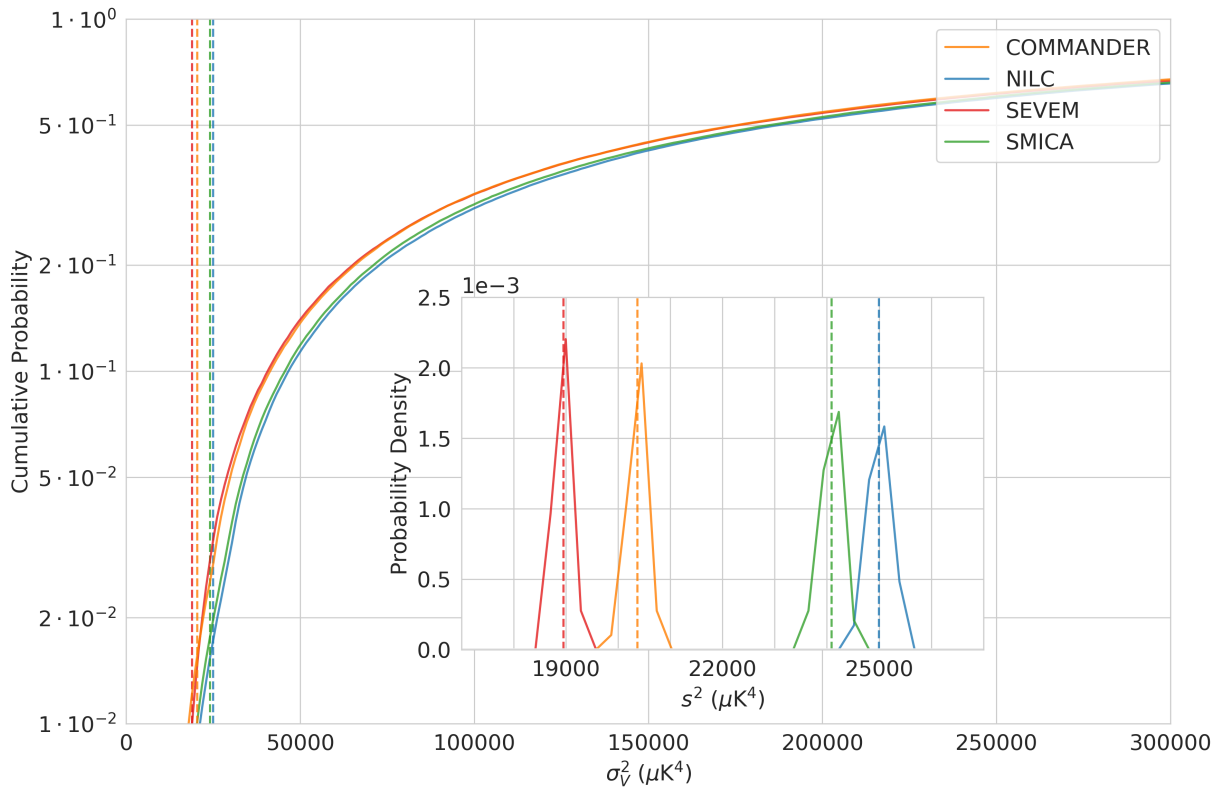


FIG. 4. The variance of great-circle variances σ_V^2 for each dipole-free $\ell \leq 3$ *Planck* map is compared against σ_V^2 for 100,000 simulations created by adding a standard model dipole \mathcal{D}_S to that particular map. Each $\ell \leq 3$ *Planck* map's set of simulations is used to create a cumulative distribution function, and at each point on this function, the cumulative probability density is the proportion of simulations of each $\ell \leq 3$ *Planck* map with values of σ_V^2 less than the value of σ_V^2 at that point. The inset shows the spread in sample variance s^2 for each dipole-free $\ell \leq 3$ *Planck* map, calculated from 100 different sets of 20,000 uniformly distributed random great circles. In both plots, the vertical lines indicate the value of σ_V^2 for each dipole-free $\ell \leq 3$ *Planck* map, calculated as the mean value of s^2 from each map's spread of sample variances. Thus, the vast majority of standard model dipoles only increase σ_V^2 when added to the dipole-free $\ell \leq 3$ sky, demonstrating that the inferred dipole that allows the great-circle variances to be as uniform in Fig. 3 is not a common occurrence in the standard model.

systematic error.

B. Harmonic analysis

To perform the spherical-harmonic decomposition of δT for each \mathcal{M} , we used the *HEALPix* function `map2alm` to calculate the $a_{\ell m}$ components up to a cutoff of $\ell_{max} = 30$, which we used to compute the C_ℓ up to ℓ_{max} by Eq. (5). Then, we determined $C(\Theta)$ by summing Eq. (6) up to the sharp cutoff ℓ_{max} . In order to find \hat{N}_ℓ , we used a differential evolution algorithm to search the space of all possible rotated coordinate systems.

C. The Variance of Great-Circle Variances

Let X denote a sample of n_s values taken with replacement from a distribution Y . The sample variance s^2 of

X is given by

$$s^2(X) = \frac{1}{n_s - 1} \sum_{j=1}^{n_s} [X_j - \bar{X}]^2, \quad (19)$$

where \bar{X} is the sample mean,

$$\bar{X} = \frac{1}{n_s} \sum_{k=1}^{n_s} X_k. \quad (20)$$

Since $s^2(X)$ is an unbiased estimator of $\sigma^2(Y)$, we have

$$\langle s^2(X) \rangle = \sigma^2(Y), \quad (21)$$

where $\langle s^2(X) \rangle$ is the expectation value of s^2 over all possible X of same sample size n_s .

To calculate V_i , we first take a sample ($n_p = 2,000$) of evenly spaced points $\vec{x}_j \in \mathbb{R}^3$ on c_i . Then, we use the *HEALPix* function `vec2pix` to map each \vec{x}_j onto its corresponding pixel and subsequently, the value $\delta T(\vec{x}_j)$ of the CMB temperature deviation at that pixel. Next, we

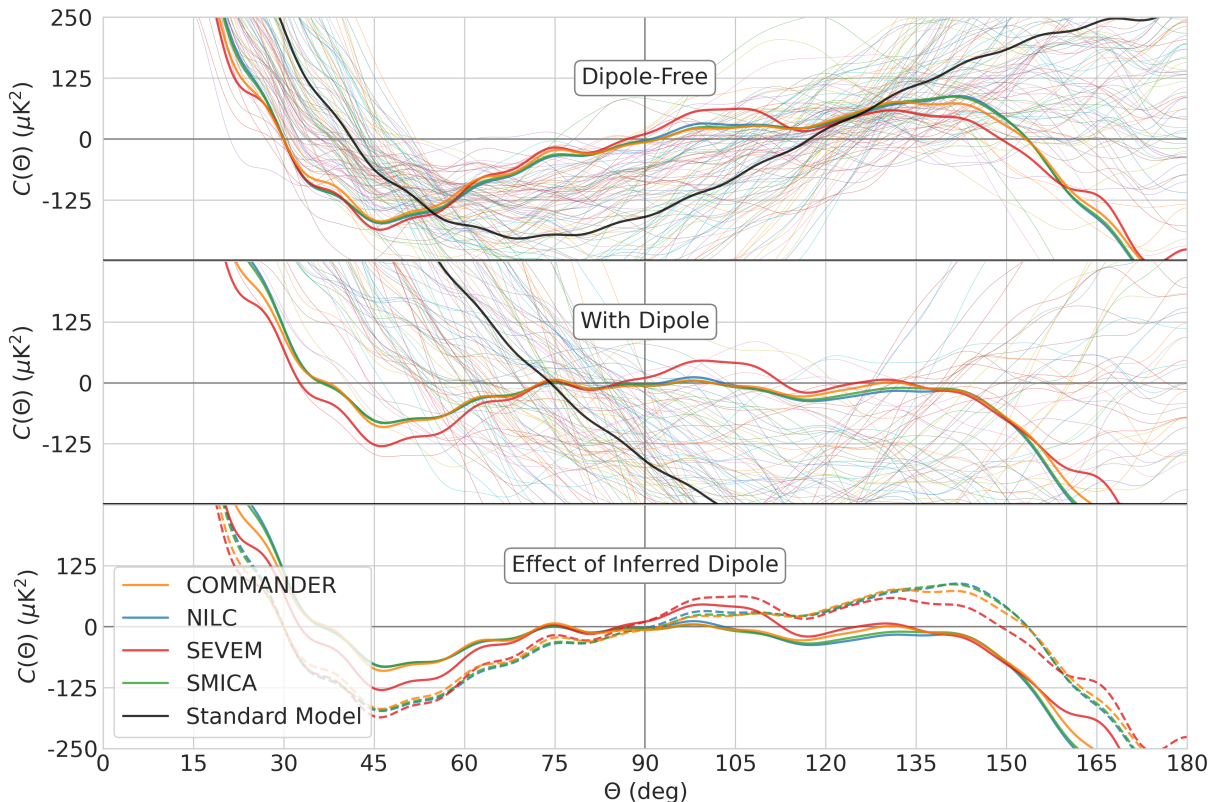


FIG. 5. Measurements and predictions for the two-point angular correlation function $C(\Theta)$, evaluated with a sharp cutoff $\ell_{max} = 30$. [Top]: The two-point angular correlation functions of the dipole-free *Planck* maps (thick colored lines) are compared to those of the dipole-free theoretical standard model expectation (thick black line) and its realizations (thin lines). [Middle]: The two-point angular correlation functions of the *Planck* maps with their inferred dipoles (thick colored lines) are compared to those of the theoretical standard model expectation with its expected dipole (thick black line), and its realizations with dipoles included (thin lines). The contrast between the two-point angular correlation functions of the *Planck* maps with their inferred dipoles and the two-point angular correlation functions predicted by the standard model illustrates the atypical nature of the inferred real sky in the standard model. [Bottom]: $C(\Theta)$ for each *Planck* map with its inferred dipole (solid lines) is compared against $C(\Theta)$ for each dipole-free *Planck* map (dashed lines). This shows how the addition of the dipole inferred from the posited great-circle variance symmetry causes $C(\Theta)$ to approximately vanish on the angular interval $\Theta = [90^\circ, 135^\circ]$. For the two-point angular correlation functions of the *Planck* maps with their inferred dipoles, the uncertainty due to the inferred dipole is small (less than $3.5 \mu\text{K}^2$ at all points).

define the sample A of n_p values A_j from the distribution δT_i as

$$A_j = \delta T(\vec{x}_j), \quad (22)$$

so $s^2(A)$ is an unbiased estimator of $\sigma^2(\delta T_i)$. Then, since $V_i = \sigma^2(\delta T_i)$, we use Eq. (21) to measure V_i as $\langle s^2(A) \rangle$, which we compute as $s^2(A)$ from a single sample A using Eq. (19).

As a check on pixelation error, we calculated V_i in the previously described manner for a set of $n_c = 20,000$ uniformly distributed random c_i on one map at two different resolutions defined by $N_{\text{side}} = 256$ and $N_{\text{side}} = 128$, respectively. In all cases, the difference in the values of V_i calculated at the different resolutions was less than 0.5%. Furthermore, to ensure sufficiently high sampling frequency of points from each great circle, we calculated V_i in the previously described manner for a set of n_c

uniformly distributed random c_i with samples of size n_p and samples of size $n_p/2$. For all great circles, the difference in the values of V_i calculated with the different sample sizes was less than 0.4%. As a check on error due to beating between the pixelation pattern and the sampling frequency of points from each great circle, we calculated V_i in the previously described manner for a set of n_c uniformly distributed random c_i with samples of size n_p and with three other slightly reduced sample sizes ($n_p - 1$, $n_p - 2$, and $n_p - 3$). For all great circles, the difference between the values of V_i calculated with the samples of size n_p and those calculated with any of the slightly reduced sample sizes was less than 0.3%.

Let B denote a sample of n_c great-circle variances V_i from V , calculated from a set of n_c uniformly distributed random c_i , so $s^2(B)$ is an unbiased estimator of σ_V^2 . Then, since $\sigma_V^2 = \sigma^2(V)$, we use Eq. (21) to measure

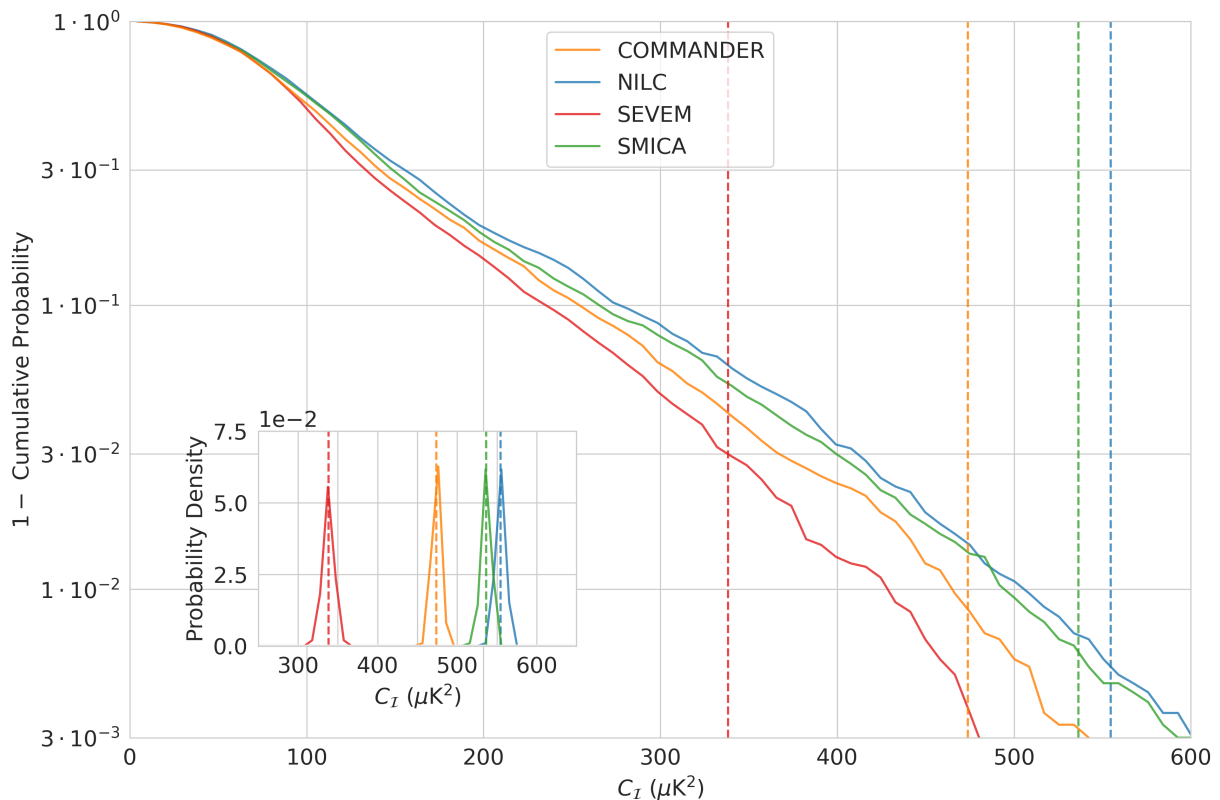


FIG. 6. The inferred dipole amplitude $C_{\mathcal{I}}$ for each $\ell \leq 3$ *Planck* map (vertical lines) is compared with $C_{\mathcal{I}}$ for 3,000 same-spectrum realizations of that map. Each $\ell \leq 3$ *Planck* map's set of realizations is used to create a reverse cumulative distribution function, and the cumulative probability density is the proportion of same-spectrum realizations of each $\ell \leq 3$ *Planck* map with values exceeding $C_{\mathcal{I}}$. The inset shows the spread in values of $C_{\mathcal{I}}$ for 100 different $\mathcal{D}_{\mathcal{I}}$ for each $\ell \leq 3$ *Planck* map, calculated from 100 different sets of 20,000 uniformly distributed random great circles. In both plots, the vertical line indicates the mean value of $C_{\mathcal{I}}$ from each $\ell \leq 3$ *Planck* map's spread of inferred dipole amplitudes. Thus, the inferred intrinsic dipole that best fulfills the candidate symmetry of constant variance along great circles approximately cancels the two-point angular correlation function over the interval $\Theta = [90^\circ, 135^\circ]$ in only a very small subset of standard model realizations.

σ_V^2 as $\langle s^2(B) \rangle$. For the inferred and dipole-free version of each $\ell \leq 3$ *Planck* map, we compute $\langle s^2(B) \rangle$ as the mean value of $s^2(B)$ for 100 different samples B , where $s^2(B)$ is calculated using Eq. (19); however, for $\ell \leq 3$ *Planck* maps that have had a standard model dipole \mathcal{D}_S added and for all other simulated realizations of the CMB sky, we measure $\langle s^2(B) \rangle$ as $s^2(B)$ from a single sample B , where $s^2(B)$ is calculated using Eq. (19). As a check on the error from the finite number of great circles sampled, the spreads in the values of s^2 for the inferred and dipole-free version of each $\ell \leq 3$ *Planck* map are visible in the insets of Figs. 3 and 4, respectively.

D. The inferred dipole

To find $\mathcal{D}_{\mathcal{I}}(\mathcal{M})$, we use a differential evolution algorithm to search the space of all dipoles whose amplitudes are less than $3,000 \mu\text{K}^2$ for the \mathcal{D} that minimizes $\sigma_V^2(\mathcal{M}'_3 + \mathcal{D})$. We determined that, in practice, this space contains all possible values of $C_{\mathcal{I}}$ for the maps examined

in this paper.

When calculating $\mathcal{D}_{\mathcal{I}}$, there is some error in each of the measurements of σ_V^2 made during differential evolution, which leads to some error in $\mathcal{D}_{\mathcal{I}}$. As a check on this error, $\mathcal{D}_{\mathcal{I}}$ was measured for each *Planck* map with 100 different sets of 20,000 uniformly distributed random great circles. In the inset of Fig. 6, we show the resulting spread of $C_{\mathcal{I}}$ values. Moreover, in all cases, the resulting spread in the value of $\hat{\Omega}_{\mathcal{I}}$ for each *Planck* map is less than $\pm 1.1^\circ$ of angular distance from the mean direction of $\hat{\Omega}_{\mathcal{I}}$ for that map. To create the inferred version of each *Planck* map, we use the mean values of $C_{\mathcal{I}}$ and $\hat{\Omega}_{\mathcal{I}}$ from this ensemble of calculations. For each simulated realization of the CMB sky, we perform single calculations of $\mathcal{D}_{\mathcal{I}}$ from one set of 20,000 uniformly distributed random great circles to keep computational expense manageable.

E. Standard Model realizations

We used the *Code for Anisotropies in the Microwave Background* [20] to calculate C_ℓ^{SM} with the following six cosmological parameters from the *Planck* collaboration [21]: dark matter density $\Omega_c h^2 = 0.120$; baryon density $\Omega_b h^2 = 0.0224$; Hubble constant $H_0 = 67.4$; reionization optical depth $\tau = 0.054$; neutrino mass $m_\nu = 0.06$ eV; and spatial curvature $\Omega_k = 0.001$. For each standard model realization, we calculated the angular power spectrum up to a cutoff of $\ell_{max} = 30$ by Eq. (5). Then, we determined $C(\Theta)$ by summing Eq. (6) up to the sharp cutoff ℓ_{max} .

IV. RESULTS

A. Variance of great-circle variances on large angular scales

We begin by comparing the value of σ_V^2 for each inferred $\ell \leq 3$ *Planck* map to values of σ_V^2 from a set of that particular map's same-spectrum realizations. The results in Fig. 3 demonstrate that only a small fraction of the same-spectrum realizations have a value of σ_V^2 as low as those of their respective inferred $\ell \leq 3$ *Planck* maps, and that for the vast majority of same-spectrum realizations, the value of σ_V^2 is far higher. This indicates that the inferred $\ell \leq 3$ real sky is anomalous in the sense that its variance of great-circle variances is far below those of an overwhelming majority of same-spectrum realizations. It is even more anomalous in the complete space of standard model realizations, since these same-spectrum realizations represent a subset of standard model realizations that, in general, have far lower variance of great-circle variances than most standard model realizations.

In Fig. 4, we show that nearly all standard model dipoles increase the value of σ_V^2 when added to the dipole-free $\ell \leq 3$ sky. This demonstrates that the inferred dipole that allows the value of σ_V^2 to be so anomalous in Fig. 3 is not at all a common occurrence in the standard model. Thus, not only is variance of great-circle variances anomalously low for the inferred $\ell \leq 3$ sky, but the inferred dipole itself is anomalous in the sense that the occurrence of a dipole that reduces the variance of great-circle variances in the $\ell \leq 3$ sky is very rare in standard realizations.

B. Two-point angular correlation function including the inferred dipole

Fig. 5 shows how the addition of the dipole inferred from the posited great-circle variance symmetry causes $C(\Theta)$ to approximately vanish on the angular domain $\Theta = [90^\circ, 135^\circ]$, another symmetry predicted in some holographic quantum inflation scenarios. This agreement supports the consistency of the holographic hypothesis.

The inferred dipole uncertainty in Fig. 5 is calculated in the following manner using the Commander *Planck* map; however, we have verified that this process produces virtually the same curve, regardless of the choice of particular *Planck* map. First, we measure $\mathcal{D}_{\mathcal{I}}$ 100 times using 100 different sets of 20,000 uniformly distributed random great circles. This produces an ensemble of 100 different values of $C_{\mathcal{I}}$, which allows us to calculate a mean value of $C_{\mathcal{I}}$. Additionally, there is a $C_{\mathcal{I}}$ that has the greatest absolute deviation from this mean value of $C_{\mathcal{I}}$. The inferred dipole uncertainty is calculated as the absolute value of the two-point angular correlation function calculated from the mean value of $C_{\mathcal{I}}$ minus the two-point angular correlation function calculated from the value of $C_{\mathcal{I}}$ that has the greatest absolute deviation from the mean value of $C_{\mathcal{I}}$.

In Fig. 6, we demonstrate that the amplitude $C_{\mathcal{I}}$ of the inferred dipole for same-spectrum realizations of our $\ell \leq 3$ sky is almost always lower than that measured for our real sky, and therefore, does not cause the vanishing of the two-point angular correlation function at large angles. All same-spectrum realizations that had higher or comparable inferred dipole amplitude to our sky had very nearly the same detailed characteristics as our sky: a highly sectoral octupole moment, and high alignment between the quadrupole and octupole (the exception to this is SEVEM, which had several realizations with less alignment between the quadrupole and octupole). Thus, our sky is extremely uncommon in that it is one of the few skies in which the symmetries predicted by the holographic model are self-consistent.

C. Anomalous alignments and shapes in the natural coordinate system

Fig. 1 shows the low ℓ harmonic components of the inferred version of Commander in Galactic coordinates. Additionally, it demonstrates the close agreement between all four *Planck* maps on the inferred dipole axis $\hat{\Omega}_{\mathcal{I}}$, and the proximity of the octupole axis of maximum sectorality \hat{N}_3 to $\hat{\Omega}_{\mathcal{I}}$ for each *Planck* map.

In Fig. 2, the equirectangular projections of the low ℓ harmonic components of the inferred version of Commander in its natural coordinate system illustrate the correlations between the octupole, quadrupole, and inferred dipole of our CMB sky. On the inferred dipole, the great circles that intersect the dipole's poles all have the same, maximal variance, while the equatorial and near-equatorial great circles have no variance and very little variance, respectively. On the quadrupole moment and the highly sectoral octupole moment, the great circles that intersect the poles all have relatively little variance, while the near-equatorial great circles have near-maximal variance. As a result, the quadrupole and octupole must be aligned with the inferred dipole and the octupole must be highly sectoral in order to create variance along the near-equatorial great circles and bring the V_i closer to

being constant, thus lowering σ_V^2 . Equivalently, $\hat{\Omega}_I$ must be close to the respective axes of maximum sectorality for the quadrupole and the octupole, and the octupole must have a high maximum value of S_3 .

D. Summary

The analysis presented here shows that several known anomalies of large-angle CMB anisotropy may be related to a universal symmetry of the primordial pattern of curvature perturbations, a causal universality of great circle variance on inflationary horizons. This simple geometrical symmetry approximately accounts for several known properties in the CMB sky that are disconnected statistical anomalies in the standard model. We have shown that very few random combinations of independent $a_{\ell m}$ components drawn from the standard expected distribution agree with the posited symmetry better than the combination present in our sky.

Our results lend support to a new interpretation of long-studied large-angle CMB anomalies [15]: several of them may not be independent random statistical flukes, but may be related signatures of new physics not currently included in the standard quantum system used to

describe inflation. The results presented here are not conclusive, but are striking enough to warrant additional studies. More precise tests are currently limited by noise introduced by Galactic foreground models. One promising path forward to improve these would be better multi-frequency maps, preferably over the entire sky. New all sky experiments, in particular PIXIE [22, 23], will provide all-sky CMB maps with well controlled large angular scale systematics and very broad spectral coverage to markedly reduce the uncertainties in the low- ℓ CMB structure.

ACKNOWLEDGMENTS

This work was supported by the Fermi National Accelerator Laboratory (Fermilab), a U.S. Department of Energy, Office of Science, HEP User Facility, managed by Fermi Research Alliance, LLC (FRA), acting under Contract No. DE-AC02-07CH11359. We acknowledge the use of HEALPix/healpy and the NASA/IPAC Infrared Science Archive, which is operated by the Jet Propulsion Laboratory, California Institute of Technology, under contract with the National Aeronautics and Space Administration.

-
- [1] Planck Collaboration, “Planck 2018 results. I. Overview and the cosmological legacy of Planck,” *Astron. Astrophys.* **641**, A1 (2020), arXiv:1807.06205 [astro-ph.CO].
- [2] Angelica de Oliveira-Costa, Max Tegmark, Matias Zaldarriaga, and Andrew Hamilton, “The significance of the largest scale cmb fluctuations in wmap,” *Physical Review D* **69** (2004), 10.1103/PhysRevD.69.063516.
- [3] C. L. Bennett, R. S. Hill, G. Hinshaw, D. Larson, K. M. Smith, J. Dunkley, B. Gold, M. Halpern, N. Jarosik, A. Kogut, E. Komatsu, M. Limon, S. S. Meyer, M. R. Nolte, N. Odegard, L. Page, D. N. Spergel, G. S. Tucker, J. L. Weiland, E. Wollack, and E. L. Wright, “Seven-year wilkinson microwave anisotropy probe (wmap) observations: Are there cosmic microwave background anomalies?” *The Astrophysical Journal Supplement Series* **192**, 17 (2011).
- [4] Planck Collaboration, “Planck 2015 results. XVI. Isotropy and statistics of the CMB,” *Asro* **594**, A16 (2016), arXiv:1506.07135 [astro-ph.CO].
- [5] Dominik J. Schwarz, Craig J. Copi, Dragan Huterer, and Glenn D. Starkman, “CMB anomalies after Planck,” *Classical and Quantum Gravity* **33**, 184001 (2016), arXiv:1510.07929 [astro-ph.CO].
- [6] Planck Collaboration, “Planck 2018 results: Vii. isotropy and statistics of the cmb,” *Astron. Astrophys.* **641**, A7 (2020).
- [7] E. L. Wright, S. S. Meyer, C. L. Bennett, N. W. Boggess, E. S. Cheng, M. G. Hauser, A. Kogut, C. Lineweaver, J. C. Mather, G. F. Smoot, R. Weiss, S. Gulkis, G. Hinshaw, M. Janssen, T. Kelsall, P. M. Lubin, Jr. Moseley, S. H., T. L. Murdock, R. A. Shafer, R. F. Silverberg, and D. T. Wilkinson, “Interpretation of the Cosmic Microwave Background Radiation Anisotropy Detected by the COBE Differential Microwave Radiometer,” *Astrophys. J.* **396**, L13 (1992).
- [8] C. L. Bennett, A. Kogut, G. Hinshaw, A. J. Banday, E. L. Wright, K. M. Gorski, D. T. Wilkinson, R. Weiss, G. F. Smoot, S. S. Meyer, J. C. Mather, P. Lubin, K. Loewenstein, C. Lineweaver, P. Keegstra, E. Kaita, P. D. Jackson, and E. S. Cheng, “Cosmic Temperature Fluctuations from Two Years of COBE Differential Microwave Radiometers Observations,” *Astrophys. J.* **436**, 423 (1994), arXiv:astro-ph/9401012 [astro-ph].
- [9] Craig J. Copi, Dragan Huterer, Dominik J. Schwarz, and Glenn D. Starkman, “Large-angle anomalies in the cmb,” *Advances in Astronomy* **2010**, 847541 (2010).
- [10] Ray Hagimoto, Craig Hogan, Collin Lewin, and Stephan S. Meyer, “Symmetries of CMB temperature correlation at large angular separations,” *The Astrophysical Journal* **888**, L29 (2020).
- [11] Craig J. Copi, Dragan Huterer, Dominik J. Schwarz, and Glenn D. Starkman, “Large-scale alignments from WMAP and Planck,” *MNRAS* **449**, 3458–3470 (2015), arXiv:1311.4562 [astro-ph.CO].
- [12] Jaiseung Kim and Pavel Naselsky, “Anomalous parity asymmetry of wmap 7-year power spectrum data at low multipoles: Is it cosmological or systematics?” *Phys. Rev. D* **82**, 063002 (2010).
- [13] Craig Hogan, “Nonlocal entanglement and directional correlations of primordial perturbations on the inflationary horizon,” *Phys. Rev. D* **99**, 063531 (2019).
- [14] Craig Hogan, “Pattern of perturbations from a coherent quantum inflationary horizon,” *Classical and Quantum Gravity* **37**, 095005 (2020).

- [15] Craig Hogan and Stephan S. Meyer, “Angular correlations of causally-coherent primordial quantum perturbations,” (2021), arXiv:2109.11092 [gr-qc].
- [16] Tom Banks and W. Fischler, “The holographic spacetime model of cosmology,” *Int. J. Mod. Phys. D* **27**, 1846005 (2018), arXiv:1806.01749 [hep-th].
- [17] Tom Banks, “Holographic Space-time and Quantum Information,” *Front. in Phys.* **8**, 111 (2020), arXiv:2001.08205 [hep-th].
- [18] Thomas Banks and Kathryn M. Zurek, “Conformal Description of Near-Horizon Vacuum States,” (2021), arXiv:2108.04806 [hep-th].
- [19] K. M. Gorski, E. Hivon, A. J. Banday, B. D. Wandelt, F. K. Hansen, M. Reinecke, and M. Bartelmann, “HEALPix: A framework for high-resolution discretization and fast analysis of data distributed on the sphere,” *The Astrophysical Journal* **622**, 759–771 (2005).
- [20] Antony Lewis and Anthony Challinor, “CAMB: Code for Anisotropies in the Microwave Background,” (2011), ascl:1102.026.
- [21] Planck Collaboration, “Planck 2018 results. VI. Cosmological parameters,” *Astron. Astrophys.* **641**, A6 (2020), arXiv:1807.06209 [astro-ph.CO].
- [22] A. Kogut, D. J. Fixsen, D. T. Chuss, J. Dotson, E. Dwek, M. Halpern, G. F. Hinshaw, S. M. Meyer, S. H. Moseley, M. D. Seiffert, D. N. Spergel, and E. J. Wollack, “The Primordial Inflation Explorer (PIXIE): a nulling polarimeter for cosmic microwave background observations,” *JCAP* **2011**, 025 (2011), arXiv:1105.2044 [astro-ph.CO].
- [23] A. Kogut and D. J. Fixsen, “Calibration method and uncertainty for the primordial inflation explorer (PIXIE),” *JCAP* **2020**, 041 (2020), arXiv:2002.00976 [astro-ph.IM].